SCIENTIFIC REPORTS

OPEN

# All Nonmetal Resistive Random Access Memory

Te Jui Yen[1], Andrei Gismatulin[2], Vladimir Volodin[2,3], Vladimir Gritsenko[2,3,4] & Albert Chin[1]

Received: 22 November 2018
Accepted: 4 April 2019
Published online: 16 April 2019

**Traditional Resistive Random Access Memory (RRAM) is a metal-insulator-metal (MIM) structure, in which metal oxide is usually used as an insulator. The charge transport mechanism of traditional RRAM is attributed to a metallic filament inside the RRAM. In this paper, we demonstrated a novel RRAM device with no metal inside. The $N^+$-Si/$SiO_x$/$P^+$-Si combination forms a $N^+IP^+$ diode structure that is different from traditional MIM RRAM. A large high-resistance/low-resistance window of $1.9 \times 10^4$ was measured at room temperature. A favorable retention memory window of $1.2 \times 10^3$ was attained for $10^4$ s at 85 °C. The charge transport mechanism of virgin, high- and low-resistance states can be well modeled by the single Shklovskii-Efros percolation mechanism rather than the charge transport in metallic filament. X-ray photoelectron spectroscopy demonstrated that the value of x in $SiO_x$ was 0.62, which provided sufficient oxygen vacancies for set/reset RRAM functions.**

Resistive Random Access Memory (RRAM)[1–23] is the highly promising candidate for the next generation nonvolatile memory (NVM), because conventional charge-based memories, namely dynamic random access memory and flash memory, have too low capacitance after continuously downscaling into 1X-nm regimes. In addition, an RRAM array can be fabricated in the back end of line of a complementary metal-oxide-semiconductor circuit, which makes such device an excellent candidate for embedded NVM (eNVM) application. The typical write speed of RRAM device ranges from 100 ns to 1 μs, which is three-to-four orders of magnitude faster than flash memory. Such high-speed and process-compatible eNVM can enable hardware technologies such as artificial intelligence and neuromorphic computing[1,6–8].

The charge transport mechanism of RRAM, however, is not fully understood, and it is generally attributed to charge transport in metallic filament because of its metal–insulator–metal (MIM) structure, where the insulator is usually formed by metal oxide–based dielectric. Previously we pioneered nonmetal $GeO_x$ RRAM, but the metal electrodes used might have contributed to the charge transport mechanism[16–21]. In the paper, we report the all nonmetal RRAM that does not contain any metal in both the electrodes and dielectric insulator. The purpose of all nonmetal RRAM device is to provide a different charge transport mechanism rather than the charge transport in normal metallic filament. Relatively small device variation and tight distribution can be reached in similar $GeO_x$ RRAM[16] that are crucial for array design[17]. After forming the RRAM device under 6 V and 100 μA current compliance, a large resistance window of $1.9 \times 10^4$ was measured at room temperature (RT), which decreases slightly to $8.7 \times 10^3$ after $10^4$ s data retention. The set/reset charge transport for low- and high-resistance states (LRS and HRS), deduced from the measured current–voltage (*I–V*) characteristics, is attributed to the charge transport mechanism by Shklovskii-Efros (S-E) percolation model.

## Results

Figure 1 depicts the measured *I-V* characteristics of an $N^+$-Si/$SiO_x$/$P^+$-Si RRAM device. During the forming step, the device was first subjected to a 6 V and 100 μA compliance current stress to attain the LRS. The same device was reset into HRS after a negative voltage bias. Then, the device was set to LRS again under a positive voltage bias. However, the positive set voltage was lower than the forming voltage once the RRAM switching function was established.

The charge transport mechanism is crucial for RRAM devices. To understand the charge transport mechanism in this completely nonmetal RRAM, we further analyzed the measured *I-V* curves at different temperatures. Figure 2(a–c) depict the measured and modeled *I-V* curves in the virgin state (VS), HRS and LRS conditions, respectively. All state the HRS and LRS currents adhere to the Shklovskii-Efros (S-E) percolation model:

[1]Department of Electronics Engineering, National Chiao Tung University, Hsinchu, 300, Taiwan. [2]Rzhanov Institute of Semiconductor Physics, Siberian Branch, Russian Academy of Sciences, Novosibirsk, Russia. [3]Novosibirsk State University, Pirogova street, 2, Novosobirsk, 630090, Russia. [4]Novosibirsk State Technical University, K. Marx ave., 20, Novosibirsk, 630073, Russia. Correspondence and requests for materials should be addressed to A.C. (email: achin@faculty.nctu.edu.tw)

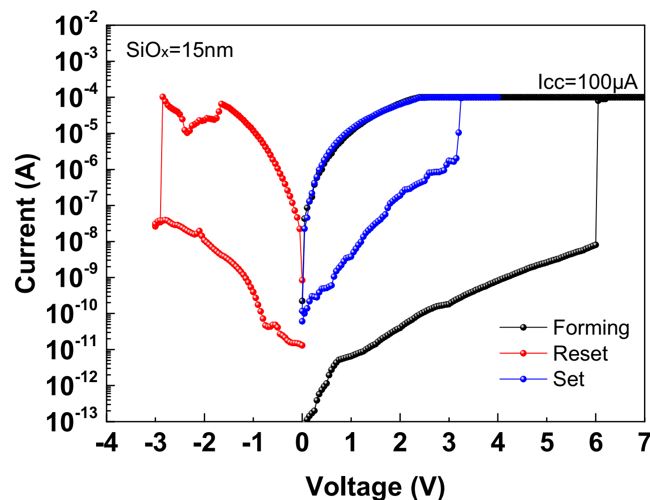


**Figure 1.** *I-V* characteristics of $N^+$-Si/$SiO_x$/$P^+$-Si RRAM device under forming, set and reset operations.

$$I = I_0 \exp\left(-\frac{W_e - \left(Ce^{\frac{U}{d}} a V_0^{\gamma}\right)^{\frac{1}{1+\gamma}}}{kT}\right), \tag{1}$$

where $I_0$, $W_e$, $a$, $V_0$, $C$ and $\gamma$ are the preexponential factor, percolation energy, space scale of fluctuations, energy fluctuation amplitude, numeric constant and it is equal to 0.25, critical index and it is equal to 0.9, respectively. The simulation by the S-E model gives reasonable model parameters to all resistance state (Fig. 2). The percolation energy decreases with decreasing resistance. Also, in the S-E model for LRS, the active contact area reduction of the charge involved in the transport is taken into account. The relation $a \times V_0^{0.52} = 1 \times 10^{-7}$ cm·eV$^{0.52}$ does not change from resistance to resistance. This is due to the fact that with decreasing resistance increases space scale of fluctuations $a$ but decreases energy fluctuation amplitude $V_0$. In addition, it can be said that the S-E percolation model is applicable to the LRS case, then it can be assumed that the conducting channel is not continuous. Hence, the results demonstrate that the charge transport of the $N^+$-Si/$SiO_x$/$P^+$-Si RRAM in VS, HRS and LRS are described by the S-E percolation model. For more details on other models and their inapplicability to HRS, see the ref.[24].

To further understand the device characteristics, material analyses were performed. Figure 3 displays the cross-sectional transmission electron microscope (TEM) image of this RRAM device. As depicted, the RRAM device was fabricated directly on a $P^+$-Si substrate, followed by a 15-nm thick $SiO_x$ dielectric layer and a $N^+$-Si top electrode. The $SiO_x$ layer was further analyzed using X-ray photoelectron spectroscopy (XPS). The sample surface was pre-sputtered to ensure that the native oxide did not influence the measurements. Figure 4 displays the XPS spectrum. From the peaks of O1s, Si2s, and Si2p, the mole fraction x in $SiO_x$ was determined to be 0.62. Because no metal or metallic ions were present in the whole RRAM device, metallic filaments were not formed[13–16]. In accordance with XPS experimental data certain fraction of vacancies exist in dielectric immediately after synthesis. The migration of oxygen vacancies plays an important role for current conduction.

Figure 5 plots potential switching mechanisms. During the forming step, the current conducted through the initial $V_o^{2+}$ inside the $SiO_x$ layer[14]. When the RRAM device was under sufficiently high positive voltage, soft breakdown in $SiO_x$ occurred and disrupted the covalent bonds[25,26], generating unbonded Si ions, $O^{2-}$ and $V_o^{2+}$. In refs.[27,28], it was shown that $V_o^{2+}$ and $O^{2-}$ anti-Frenkel pairs are not stable and should recombine immediately. We assume, that after generation of anti-Frenkel pairs, electrons are redistributed to maintain charge neutrality and new oxygen vacancies ($V_o^0$) and interstitial oxygen atoms are formed[29]. Because the atomic size of O is significantly smaller than Si, the interstitial oxygen atoms and $V_o^0$ could migrate inside $SiO_x$ under the applied electric field. At the end of the forming process, the interstitial oxygen atoms were attracted to the positive voltage and accumulated at the interface of top $N^+$I junction. Once the conduction path was formed, electrons could transport through the $V_o^0$ creating the LRS current pass in the $SiO_x$ layer. After application of a negative voltage, interstitial oxygen atoms moved away from the top $N^+$I junction and recombined with $V_o^0$ to rupture the conduction path- the reset process. After a positive voltage was applied again, the set process behaved as the forming process to form a conduction path, but under a lower positive voltage than the forming voltage due to not all generating in forming process $V_o^0$ recombined in reset process.

Data retention is the necessary characteristics for NVM, and they are related to the nonvolatile behaviour and lifetime of an RRAM device. Figure 6 depicts the retention characteristics of the $N^+$-Si/$SiO_x$/$P^+$-Si RRAM device. The completely nonmetal RRAM device could achieve favourable retention with a slight resistive window decay from $1.9 \times 10^4$ to $8.7 \times 10^3$ at RT and $3.6 \times 10^3$ to $1.2 \times 10^3$ at 85 °C after $10^4$ s retention.

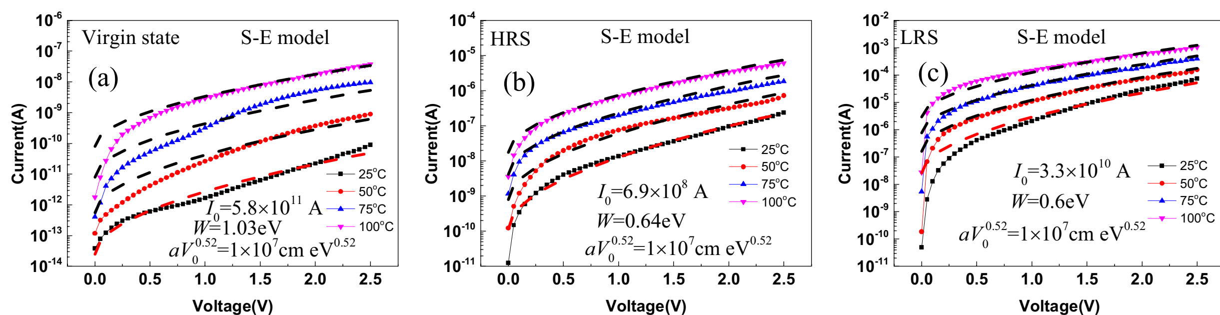


**Figure 2.** *I-V* dependences of (**a**) VS, (**b**) HRS and (**c**) LRS currents of $N^+$-Si/$SiO_x$/$P^+$-Si RRAM and fitting curves of S-E model.

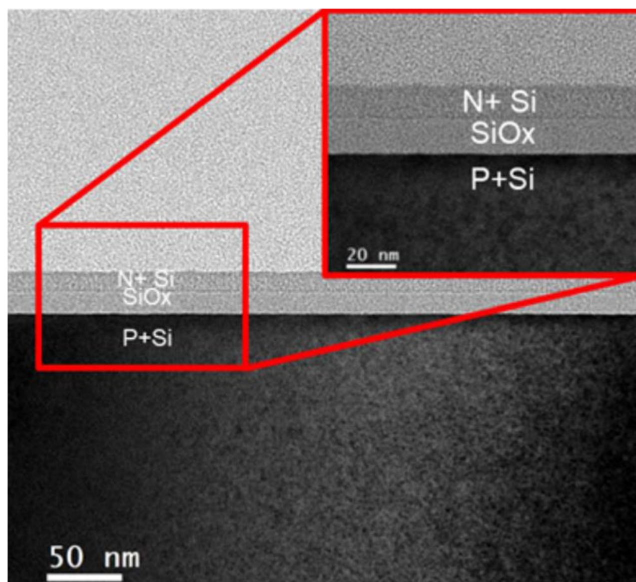


**Figure 3.** TEM image of $N^+$-Si/$SiO_x$/$P^+$-Si RRAM devices.

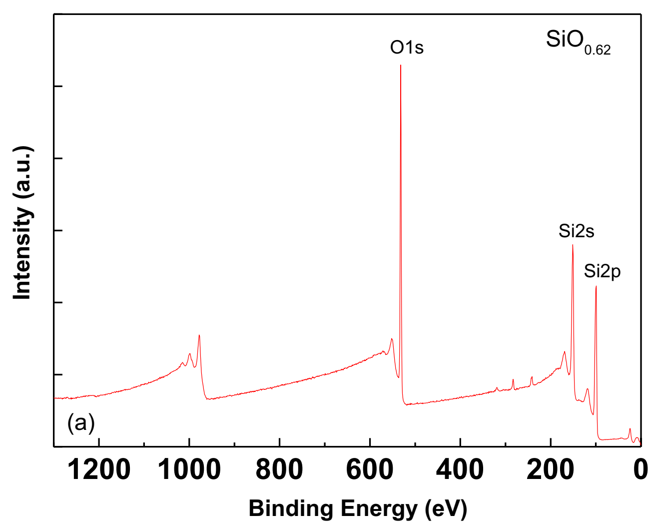


**Figure 4.** XPS spectrum of $SiO_x$ layer.

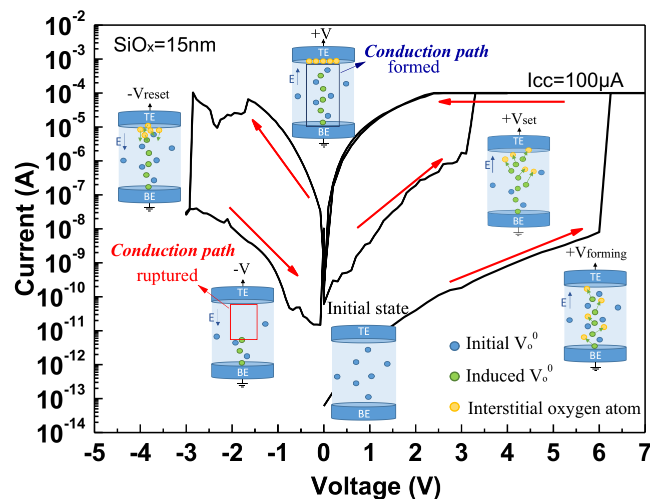


**Figure 5.** Potential microscopic conduction of $N^+$-Si/$SiO_x$/$P^+$-Si RRAM device.

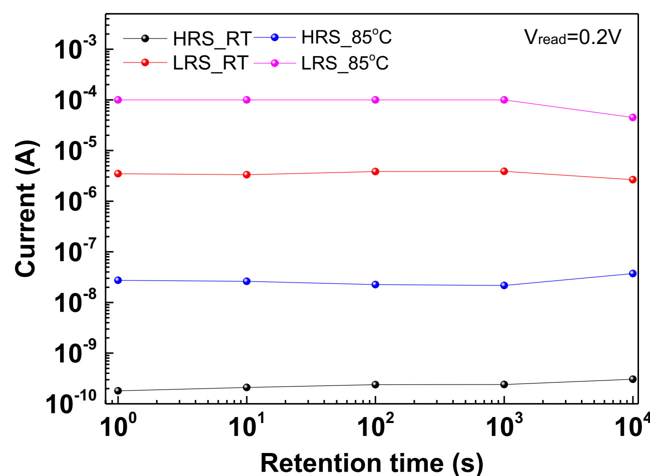


**Figure 6.** Retention characteristics of $N^+$-Si/$SiO_x$/$P^+$-Si RRAM devices at RT and 85 °C.

## Conclusion

A completely nonmetal RRAM device was demonstrated for the first time. A large resistance window of $1.9 \times 10^4$ at RT was measured. An excellent retention resistance window of $1.2 \times 10^3$ was obtained for $10^4$ s retention at 85 °C. In addition, the charge transport of the $N^+$-Si/$SiO_x$/$P^+$-Si RRAM in VS, HRS and LRS are described by the S-E percolation model. And the $V_o^0$ migration played an important role in the set/reset functions.

## Methods

The RRAM device was made on a highly doped $P^+$-Si substrate with a resistance lower than 0.01 Ω per square, which was also used as a bottom electrode. After standard RCA clean, the native oxide on $P^+$-Si wafer was removed by a dilute hydrofluoric (HF) acid (HF: $H_2O$ = 1:100) solution for 60 sec. Then, a 15-nm-thick $SiO_x$ was deposited by reactive sputtering. The composition ratio inside the $SiO_x$ was determined using XPS. Then, a 15-nm-thick amorphous $N^+$-Si layer, was formed as the top junction electrode. The diameter of the fabricated device was 120 μm. The *I-V* characteristics was measured using an HP4155B parameter analyzer. The voltage was applied on the $N^+$-Si (top electrode) side and $P^+$-Si (bottom electrode) were grounded. The sweep rate is 0.5 V/s. A Thermo K-alpha system with an X-ray spot size of 400 μm was employed for XPS measurements. The cross-sectional image of the RRAM device was measured using a JEOL 2010F high-resolution TEM. The modeled data for HRS and LRS were fitted under positive and negative voltage bias, respectively.

## References


1. Kao, B. *et al.* Modeling disorder effect of the oxygen vacancy distribution in filamentary analog RRAM for neuromorphic computing. *IEDM Tech. Dig.* 91–94 (2017).
2. Huang, P. *et al.* RTN based oxygen vacancy probing method for Ox-RRAM reliability characterization and its application in tail bits. *IEDM Tech. Dig.* 525–528 (2017).

3. Jiang, Y. *et al*. Design and Hardware Implementation of neuromorphic systems with RRAM synapses and threshold-controlled neurons for pattern recognition. *IEEE Trans. Circuits Systems I*. **65**, 2726–2738 (2018).
4. Flocke, A. & Noll, T. G. Fundamental analysis of resistive nano-crossbars for the use in hybrid nano/CMOS-memory. *European Solid State Circuits Conference* (*ESSCIRC*). 328–331 (2007).
5. Wong, H.-S. P. & Salahuddin, S. Memory leads the way to better computing. *Nat. Nanotech.* **10**, 191–194 (2015).
6. Lv, H. *et al*. BEOL Based RRAM with one extra-mask for low cost, highly reliable embedded application in 28 nm node and beyond. *IEDM Tech. Dig*. 36–39 (2017).
7. Yao, P. *et al*. Face classification using electronic synapses. *Nat. Commun.* **8**, 15199 (2017).
8. Pedretti, G. *et al*. Memristive neural network for on-line learning and tracking with brain-inspired spike timing dependent plasticity. *Sci. Rep.* **7**, 5288 (2017).
9. Li, C. *et al*. Three-dimensional crossbar arrays of self-rectifying Si/$SiO_2$/Si memristors. *Nature*. *Communications* **8**, 15666 (2017).
10. Linn, E., Rosezin, R., Kugeler, C. & Waser, R. Complementary resistive switches for passive nanocrossbar memories. *Nat. Mater.* **9**, 403–406 (2010).
11. Akinaga, H. & Shima, H. Resistive random access memory (ReRAM) based on metal oxides. *Proc. IEEE.* **98**, 2237–2251 (2010).
12. Waser, R. & Aono, M. Nanoionics-based resistive switching memories. *Nat. Mater.* **6**, 833–840 (2007).
13. Zhang, R. Characterization of oxygen accumulation in indium-tin-oxide for resistance random access memory. *IEEE Electron Device Lett.* **35**, 630–632 (2014).
14. Dong, L. P., Jia, R. X., Xin, B., Peng, B. & Zhang, Y. M. Effects of oxygen vacancies on the structural and optical properties of $\beta$-$Ga_2O_3$. *Sci. Rep.* **7**, 40160 (2017).
15. Lanza, M. *et al*. Recommended methods to study resistive switching devices. *Adv. Electron. Mater.* **5**, 1800143 (2018).
16. Chou, K. I., Cheng, C. H., Zheng, Z. W., Liu, M. & Chin, A. Ni/$GeO_x$/$TiO_y$/TaN RRAM on flexible substrate with excellent resistance distribution. *IEEE Electron Device Lett.* **34**, 505–507 (2013).
17. Chen, Y. D. & Chin, A. An offset readout current sensing scheme for one-resistor RRAM-based cross-point array. *IEEE Electron Device Lett.* **40**, 208–211 (2019).
18. Cheng, C. H., Chou, K. Y., Chin, A., Yeh, F. S. Very high performance non-volatile memory on flexible plastic substrate. *IEDM Tech. Dig*. 512–515 (2010).
19. Cheng, C. H., Chin, A. & Yeh, F. S. High performance ultra-low energy RRAM with good retention and endurance. *IEDM Tech. Dig*. 448–451 (2010).
20. Cheng, C. H., Chin, A. & Yeh, F. S. Novel ultra-low power RRAM with good endurance and retention. *Symp. on VLSI Tech. Dig*. 85–86 (2010).
21. Shaposhnikov, A. V., Perevalov, T. V., Gritsenko, V. A., Cheng, C. H. & Chin, A. Mechanism of $GeO_2$ resistive switching based on the multi-phonon assisted tunneling between traps. *Appl. Phys. Lett.* **100**, 243506 (2012).
22. Zackriya, M., Kittur, H. M. & Chin, A. A novel read scheme for large size one-resistor resistive random access memory array. *Sci. Rep.* **7**, 42375 (2017).
23. Zackriya, M., Chin, A. & Kittur, H. M. Impact of current distribution on RRAM array with high and low $I_{on}/I_{off}$ devices. *IEEE EDTM Tech. Dig*. 156–157 (2017).
24. Gismatulin, A. A. *et al*. Charge transport mechanism of high-resistive state in RRAM based on $SiO_x$. *Appl. Phys. Lett.* **114**, 033503 (2019).
25. Padovani, A., Gao, D. Z., Shluger, A. L. & Larcher, L. A microscopic mechanism of dielectric breakdown in $SiO_2$ films: An insight from multi-scale modeling. *Journal of Applied Physics.* **121**, 155101 (2017).
26. Gao, D. Z., El-Sayed, A.-M. & Shluger, A. L. A mechanism for Frenkel defect creation in amorphous $SiO_2$ facilitated by electron injection. *Nanotechnolog.* **27**, 505207 (2016).
27. Schie, M., Menzel, S., Robertson, J., Waser, R. & Souza, R. A. D. Field-enhanced route to generating anti-Frenkel pairs in $HfO_2$. *Physical review materials.* **2**, 035002 (2018).
28. Clima, S., Govoreanu, B., Jurczak, M. & Pourtois, G. $HfO_x$ as RRAM material – First principles insights on the working principles. *Microelectronic Engineering.* **120**, 13–18 (2014).
29. Mehonic, A. *et al*. Silicon Oxide ($SiO_x$): A Promising Material for Resistance Switching? *Adv. Mater*. 1801187 (2018).


## Acknowledgements

This paper's publication was supported in part by Ministry of Science and Technology of Taiwan, project no. 107-2923-E-009-001-MY3 and Russian Science Foundation (project no. 18-49-08001). We would also like to thank Damir Islamov for discussing the switching nature.

## Author Contributions

T.J. Yen did the experiments; Albert Chin is the principle investigator (PI) to write the main manuscript text; Vladimir Volodin and Vladimir Gritsenko are the co-PI's for this work. A. Gismatulin analyzed the charge transport mechanism. All authors reviewed the manuscript.

## Additional Information

**Competing Interests:** The authors declare no competing interests.

**Publisher's note:** Springer Nature remains neutral with regard to jurisdictional claims in published maps and institutional affiliations.

**Open Access** This article is licensed under a Creative Commons Attribution 4.0 International License, which permits use, sharing, adaptation, distribution and reproduction in any medium or format, as long as you give appropriate credit to the original author(s) and the source, provide a link to the Creative Commons license, and indicate if changes were made. The images or other third party material in this article are included in the article's Creative Commons license, unless indicated otherwise in a credit line to the material. If material is not included in the article's Creative Commons license and your intended use is not permitted by statutory regulation or exceeds the permitted use, you will need to obtain permission directly from the copyright holder. To view a copy of this license, visit http://creativecommons.org/licenses/by/4.0/.

© The Author(s) 2019